Supplementary Information for

Environmentally friendly thermoelectric sulphide Cu₂ZnSnS₄ single crystals with dimensionless figure of merit *ZT* achieving 1.6

Akira Nagaoka, *[a] Kenji Yoshino,[b] Taizo Masuda,[c] Taylor D. Sparks,[d] Michael A. Scarpulla[d] and Kensuke Nishioka[a]

[a]*Research Center for Sustainable Energy & Environmental Engineering, University of Miyazaki, Miyazaki 889-2192, Japan. *E-mail: nagaoka.akira.m0@cc.miyazaki-u.ac.jp*
[b]*Department of Applied Physics and Electronic Engineering, University of Miyazaki, Miyazaki 889-2192, Japan.*
[c]*S-Frontier Division, Toyota Motor Corporation, Shizuoka 411-0019, Japan.*
[d]*Department of Materials Science and Engineering, University of Utah, Salt Lake City, Utah 84112, USA.*

Single crystal growth

Traveling Heater Method (THM): It is generally difficult to grow high-quality Cu_2ZnSnS_4 (CZTS) single crystals from melt because this material grows through a peritectic reaction (liquid phase + ZnS solid phase) [S1]. On the other hand, growth by the THM based on solution growth, which can proceed below the melting point, is well-suited for high-quality CZTS single crystals.

Feed polycrystalline of CZTS was synthesized by using a melting reaction. Cu (99.999%), Zn (99.9999%), Sn (99.9999%), and S (99.999%) shots and Na_2S (99%) powder were used as starting materials. Prior to growth, Cu, Zn, and Sn were chemically etched with HCl solution for 60 s and then rinsed in ultrapure 18MOhm water. The ingots (15 g) with nominal compositions were synthesized by mixing the described amounts of elements in a carbon-coated 2 mm wall thickness quartz ampoule with 9 mm inner diameter under high vacuum of 10^{-6} Torr and then flame-sealed off. In a vertical furnace, the sealed ampoule was heated at 200 ºC/h to 650 ºC and held at this temperature for 24 h to react the constituents and prevent explosion from the S overpressure. Then the sealed ampoule was heated at 80 ºC/h to 1100 ºC and held at this temperature for 24 h to complete the reaction and ensure homogenization. The ampoule was then removed from the furnace and allowed to cool rapidly in air.

The feed polycrystalline CZTS ingot (80 mol%) and Sn solvent (20 mol%) were loaded into a carbon-coated quartz ampoule 2 mm wall thickness quartz ampoule with 10 mm inner diameter. The ampoule was flame-sealed off under high vacuum of 10^{-6} Torr, and then inserted into the THM furnace. The THM furnace has three coil heaters (upper, main, and bottom) for controlling temperature gradient. The upper heater temperature of 800 ºC was used to prevent a sulfur deficiency in the grown CZTS crystal. The sulfur species evaporated from liquid zone condensed on the cold wall of the ampoule without heating the upper part, thereby reducing the sulfur mole fraction in the crystal. For the THM growth, the main heater temperature (growth temperature) was 850 ºC which is 50 ºC higher than liquids temperature, and temperature gradient between the main and bottom heaters (the supersaturation region for single crystal growth) was about 40 ºC/cm. This temperature gradient can control the length of solution zone. The growth speed was 4-5 mm/day for 10 days. CZTS single crystals were cooled at the rate of 500 ºC/h from 700 ºC after crystal growth. The dimensions of single crystal ingot are 10 mm in diameter and 40 mm length including zone solution region.

Characterization

<u>Structural properties</u>

The combination of X-ray diffraction (XRD) and Raman spectroscopy is a useful tool for investigation of secondary phases because the XRD peaks of CZTS overlap well with those of Cu_2S and ZnS, especially. The result details of both measurements are reported in our previous papers [S2-S3]. The powder XRD pattern of each composition of samples exhibits major peaks corresponding to diffraction lines of the kesterite structure of CZTS (ICDD data #01-075-4122) in Fig. S1(a). The distinct peak at around $2\theta = 18.3º$ can be observed for distinguishing between the kesterite and stannite structures. Samples in this study have the kesterite structure without secondary phases from XRD measurement. No secondary phases, such as Cu_2SnS_3 and ZnS, were observed in Raman measurement by 532 nm excitation source, as shown in Fig. S1(b). The spectra show clearly the CZTS peaks at 287, 337, and 371 cm^{-1}. For the electrical and thermoelectric (TE) measurements, all CZTS single crystals were cut along a- and c-axes, which the (200)/(004) reflect plane can be observed by XRD in Fig. S1(c).

The quality of samples for TE measurements were evaluated by X-ray rocking curve (XRC) method shown in Fig. S2. It can be observed that the curves have good symmetry and narrow full width at half-maximum (FWHM). The results of multi-point tests on different positions of the sample wafer show that the FWHM of the (004) diffraction peak is between 106 to 140 arcsec, which means that the crystal integrity of samples 1-4 is quite good.

Compositional properties
The compositional ratios (Cu:Zn:Sn:S) of each sample are 1.97:1.04:0.97:4.02 (Sample 1), 1.85:1.06:1.02:4.07 (Sample 2), 1.83:1.07:1.01:4.09 (Sample 3), and 1.87:1.05:1.03:4.05 (Sample 4) in Table S1. In this study, our strategy for improvement of TE properties is the utilization of shallower Cu vacancy (V_{Cu}) acceptor by Cu-poor, Zn-rich condition than Cu on Zn antisite (Cu_{Zn}) for reported quaternary compounds by Cu-rich, Zn-poor condition. In addition, the concentration of unintentional impurities detected by ICP-AES is summarized in Table S2, for which the effect of Na-doping is confirmed. The unintentional impurity concentrations are fairly low (less than several hundreds of ppb level).
It is very difficult to measure the Na distribution in samples by EDX mapping because energies in the emission of characteristic X-rays for Na and Zn are overlapped. The ICP-AES measurements were performed at three points from the edges and center for wafers cut from the ingot tip at 5 mm intervals. It can be observed that Na concentration in each CZTS ingot appear to be spatially homogeneous within ±0.005 mol% by ICP-AES.

Observation of ordered-disordered transition
Temperature dependence of the specific heat C_p and thermogravimetric analysis (TGA) of stoichiometric samples with different cooling rate were shown in Fig. S4(a)-(b). The value of C_p of disordered sample increases monotonically with increasing temperature according to Dulong–Petit law, while that of ordered sample indicates small reduction between 500 K to 550 K which corresponds to the relaxation of ordered-disordered transition at reported temperature of 533 K [S4]. TGA results indicate no mass change for both samples over entire range of temperature. Considering the impact of ordered-disordered transition on TE properties, temperature dependence of Seebeck coefficient for both samples was shown in Fig. S4(c). No significant change and anisotropy of Seebeck coefficient was identified by ordered-disordered transition, however slope of both samples was different between 500 K to 600 K near critical transition temperature of 533 K which this change was also observed in CZTS polycrystalline sample [S4-S5]. We conclude that there is no significant impact of ordered-disordered transition on TE properties for CZTS material.

Thermal conductivity for high temperature region
The thermal conductivity was calculated from $\kappa = \lambda C_p D$. The thermal diffusivity coefficient λ was measured along the same direction as the electrical and TE measurements using the laser flash diffusivity method. Measurements were carried out in the range from 300-800 K.

ZT measurement uncertainty
The measurement of conductivity σ, Seebeck coefficient S, and thermal conductivity κ (calculated from λ, C_p, and D), each has an uncertainty of 2 % to 12 %. The uncertainty in dimensionless figure of merit *ZT* can be expressed as Eq. (s1) by each measurement uncertainties.

$$\frac{\Delta ZT}{ZT} = \frac{\Delta\sigma}{\sigma} + 2\frac{\Delta S}{S} + \frac{\Delta\lambda}{\lambda} + \frac{\Delta C_p}{C_p} + \frac{\Delta D}{D} \qquad (s1)$$

The multiple measurements for all properties were carried out, and then we found good repeatability. The uncertainty of σ is 4-8% (Fig. S5(a)) and S is 2-6% (Fig. S5(b)), and the measurement uncertainty of the power factor PF is 8-20% (Fig. S5(c)) by combining the uncertainties of σ and S. The uncertainty of κ is 8-12% (Fig. S6(a)) comprising those of 3-5% for λ (Fig. S6(b)), 3-5% for C_p (Fig. S6(c)), and 2% for D. The combined uncertainty for all measurements involved in the calculation of ZT is within 30 % in Fig. S7. The ZT for sample 3 (Na: 0.1 mol% doped) ranges 1.4 to 1.9 at 800 K.

Temperature dependence of mobility

The measured hole mobility data as a function of temperature for each sample in Fig. S8. First, we discuss two distinct regions roughly: the phonon scattering for high temperature ($T > 300$ K) and the ionized impurity scattering for low temperatures ($T < 100$ K) with a transition in between. The lines included in Fig. S8(a) are the fitting to $\mu \sim T^k$. The k values for low temperatures indicates more than 1.5, which suggests a hopping conduction by intrinsic point defects. The slope in the higher temperature region follows a T^{-k} behavior of a semiconductor, which means that typical lattice scattering by the acoustic phonon is dominant. The absolute k values for high temperature are higher with off-stoichiometry and Na-doping and these coincide with lower thermal conductivity.

For modeling the scattering processes of kesterite compounds, we have considered some scattering terms that is impurity, lattice, polar optical and neutral impurity scatterings from various reported results. In this study, we attempt to fit data by impurity conduction and lattice scattering processes. Because only the hopping conduction between localized states in the impurity band is dominant for the low temperature region $T < 100$ K in our previous studies [S6-S7], it is not described as typical $\sim T^k$ relation. The impurity mobility μ_I in this study are expressed as exponential function (s2) based on hopping conduction [S8]

$$\mu_I = \frac{H}{k_b T}\exp\left(-\frac{W}{k_b T}\right) \qquad (s2)$$

where H is a constant, W the hopping activation energy and k_b is Boltzmann constant. The total lattice mobility in CZTS is consisted of acoustic (AC) and non-polar (NPO) phonon scattering due to localized short-range non-cubic lattice distortions and non-parabolic valence band caused from the deformation of optical lattice, which is more dominant than polar optical scattering in p-type conduction at high temperature [S9]. This combined AC and NPO model mobility is well considered as equation (s3) [S9].

$$\mu_{AC,NPO} = 3.17 \times 10^{-5}\frac{Du^2 S(\theta,\eta,T)}{(m_{v1}/m_e)^{5/2}E_{AC}^2}T^{-3/2} \qquad (s3)$$

$$u = \frac{k_B\theta_D}{\hbar}\left(\frac{V}{6\pi^2}\right)^{1/3}$$

$$S(\theta,\eta,T) = (1 + A\eta)^{-1}$$

$$A = \frac{1.34z}{e^z - 0.914}$$

$$\eta = \left(E_{NPO}/E_{AC}\right)^2$$

where D is the density, u is the average velocity of sound, m_{v1}/m_e is the hole effective mass ratio of topmost valence band, θ_D is the Debye temperature, V is the average atomic volume, E_{AC} and E_{NPO} are the deformation potentials for the acoustic and optical phonons respectively, θ is the

characteristic temperature of the optical phonons and $z = \theta/T$. The values of D, u, θ_D and V are determined from our experimental measurements. The density of state (DOS) mas of the valence band is determined by calculation ellipsoidal expression $m_{v1} = \left(m_{v1}^{\perp} m_{v1}^{\perp} m_{v1}^{\parallel}\right)^{1/3}$. All parameters on scattering process are shown in Table S4. The total hole mobility μ of CZTS are calculated by using Mathiessen's approximation from Eqs. (s2) - (s3).

$$\frac{1}{\mu} \approx \frac{1}{\mu_I} + \frac{1}{\mu_{AC,NPO}} \qquad (s4)$$

In Fig. S8(b)-(d) the hole mobility fitted data for CZTS samples in this study are plotted by using Eq. (s4). Excellent quantitative agreements between the calculation and the experimental values over the whole temperature range have obtained for all samples. Considering high temperature region > 500 K for TE material, the lattice scattering combined with AC and NPO is most important mechanism accounting for 60 - 70% of total mobility. On the other hand, impurity conduction accounts for 30 - 40% of total mobility. Despite the increase in hole concentration, the hole mobility can be improved by off-stoichiometry and Na-doping which is because of shallower thermal energy W by screening effect [S7].

Stability for high temperature
Thermogravimetric analysis (TGA) was performed on Rigaku Thermo plys EVO2/TG-DTA under a N_2 flow in the temperature range from 300-800 K with a rate of 5 K/min in Fig. S9. The TGA results indicate that all samples are stable at the temperature up to 800 K in N_2 atmosphere.

Electronic band structures of disordered and Na-doped CZTS
We employ a 2×2×1 supercell containing 64 atom sites which is constructed by extending the optimized unit cell for disordered and Na-doping models shown in Fig. S10. The Na atom substituting on Cu 2a site (Na_{Cu} defect) is lowest formation energy where is 6.25% Na doping concentration. Fig. S11 shows the calculated electronic band structures and the calculated density of states (DOS) for the ordered, disordered and Na-doped with ordered CZTS by using density of functional theory (DFT). The increased DOS by Cu-deficit and Na-doping could be observed from experimental measurement in this study. However, there is no significant Na effect on electronic band structure and DOS in the vicinity of Γ point. The hole effective mass is slightly increased by Na-doping in Table S6. Other possible Na effect on DOS is the increasing of Na-related substitution acceptor defect such as Na substituting on Zn site (Na_{Zn}) with low formation energy or defect complex.
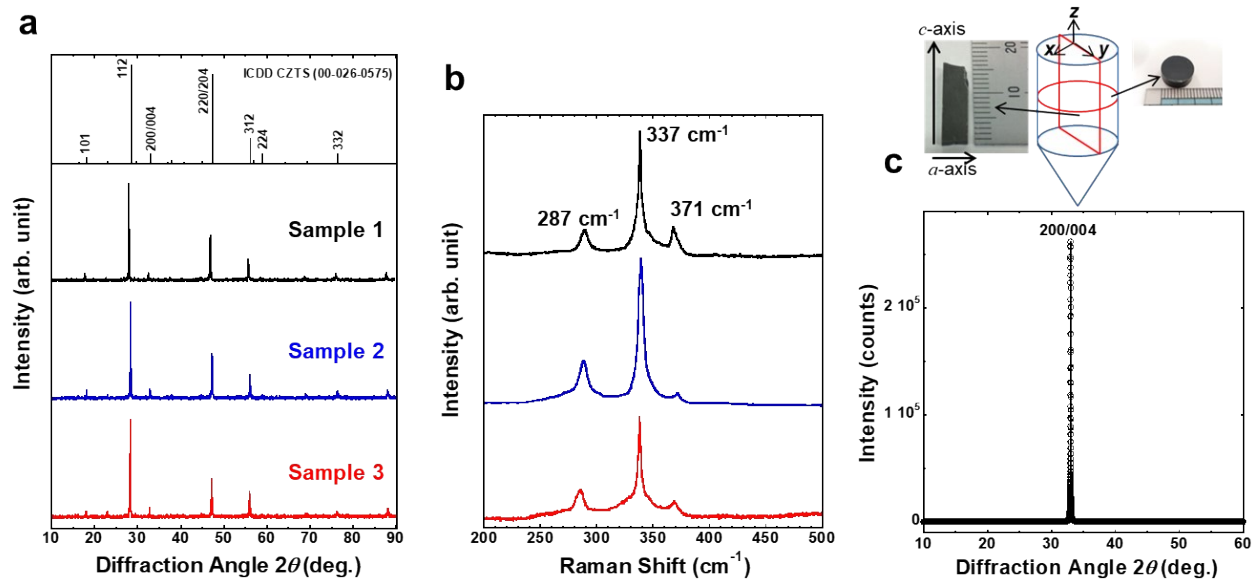
Fig. S1 Structural properties for samples 1 (stoichiometric), 2 (Cu-poor), and 3 (Na: 0.1 mol%) for confirming of kesterite phase. (a) the powder XRD patterns, (b) Raman spectroscopy, (c) XRD of the cutting plane along *a*- and *c*-axes. Inset images: how crystals were cut for directional measurements. Simulation pattern of kesterite CZTS can be obtained from Rietveld analysis of powder XRD pattern for sample 1 recorded at 300 K (R_{wp} = 6.4%, R_p = 4.3%, and R_{Bragg} = 2.4%).
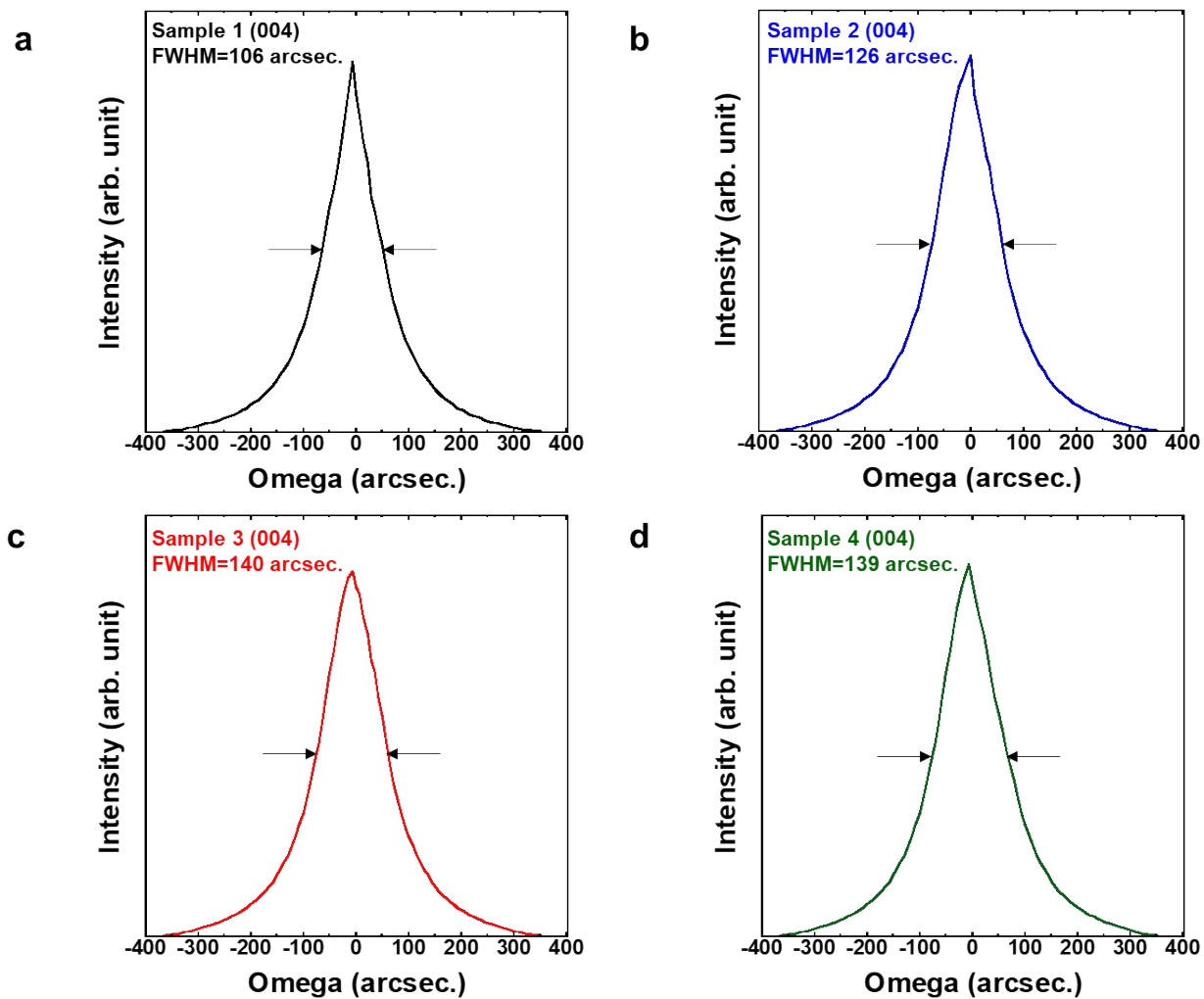
Fig. S2 XRC results of CZTS (004) wafers for crystal quality. (a) sample 1 (stoichiometric), (b) sample 2 (Cu-poor), (c) sample 3 (Na: 0.1 mol%), (d) sample 4 (Na: 0.04 mol%).
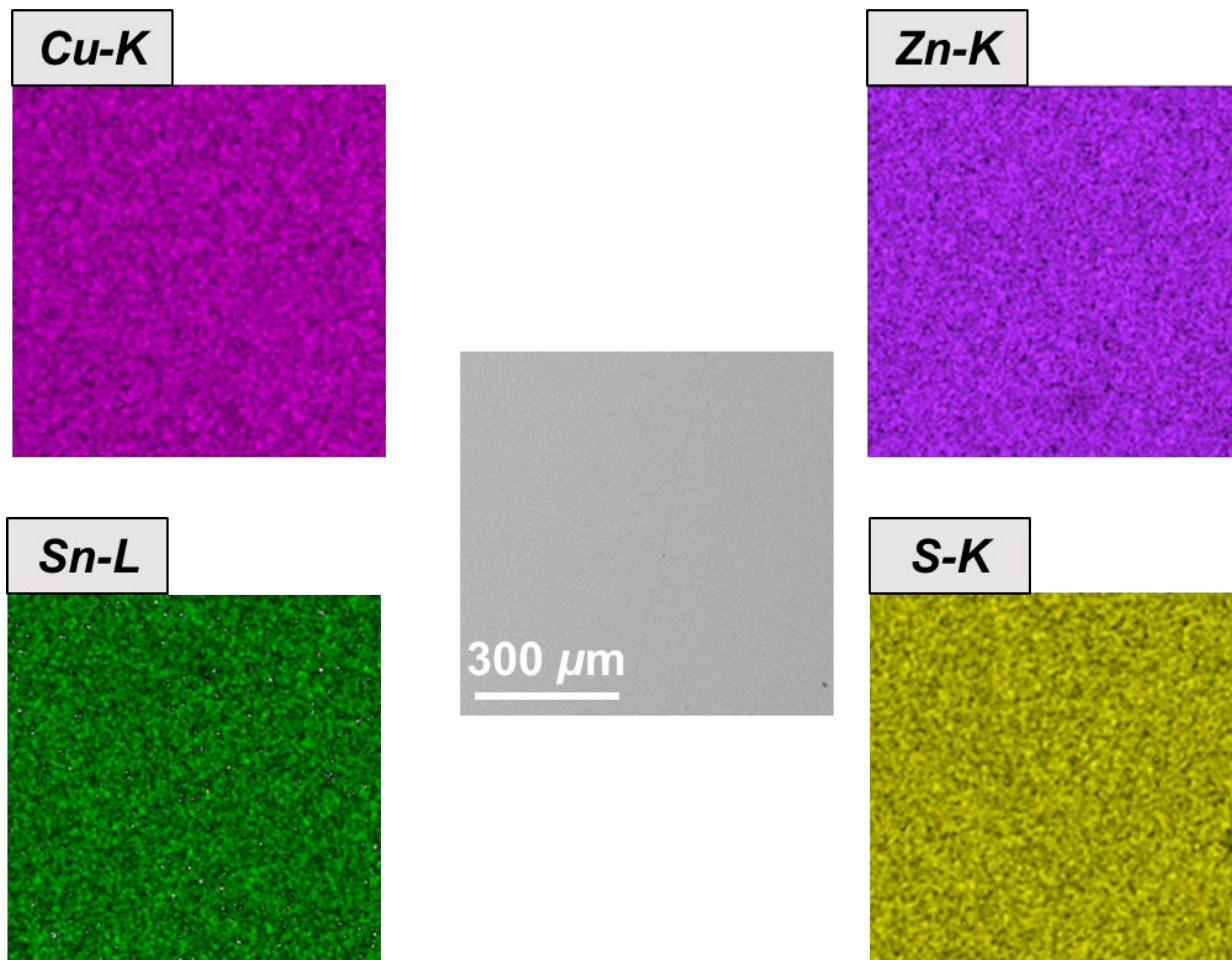
Fig. S3 The compositional homogeneity for stoichiometric CZTS single crystal by EDX mapping image at sub-millimeter scale. Stoichiometric sample 1 Cu:Zn:Sn:S = 24.6:13.0:12.2:50.2 could be observed. EDX mapping was carried out by the point-resolved Cu-K, Zn-K, Sn-L, and S-K emission lines. The compositional homogeneity of all single crystals are less than 2 at.% throughout each ingot and wafer by EDX mapping measurement.
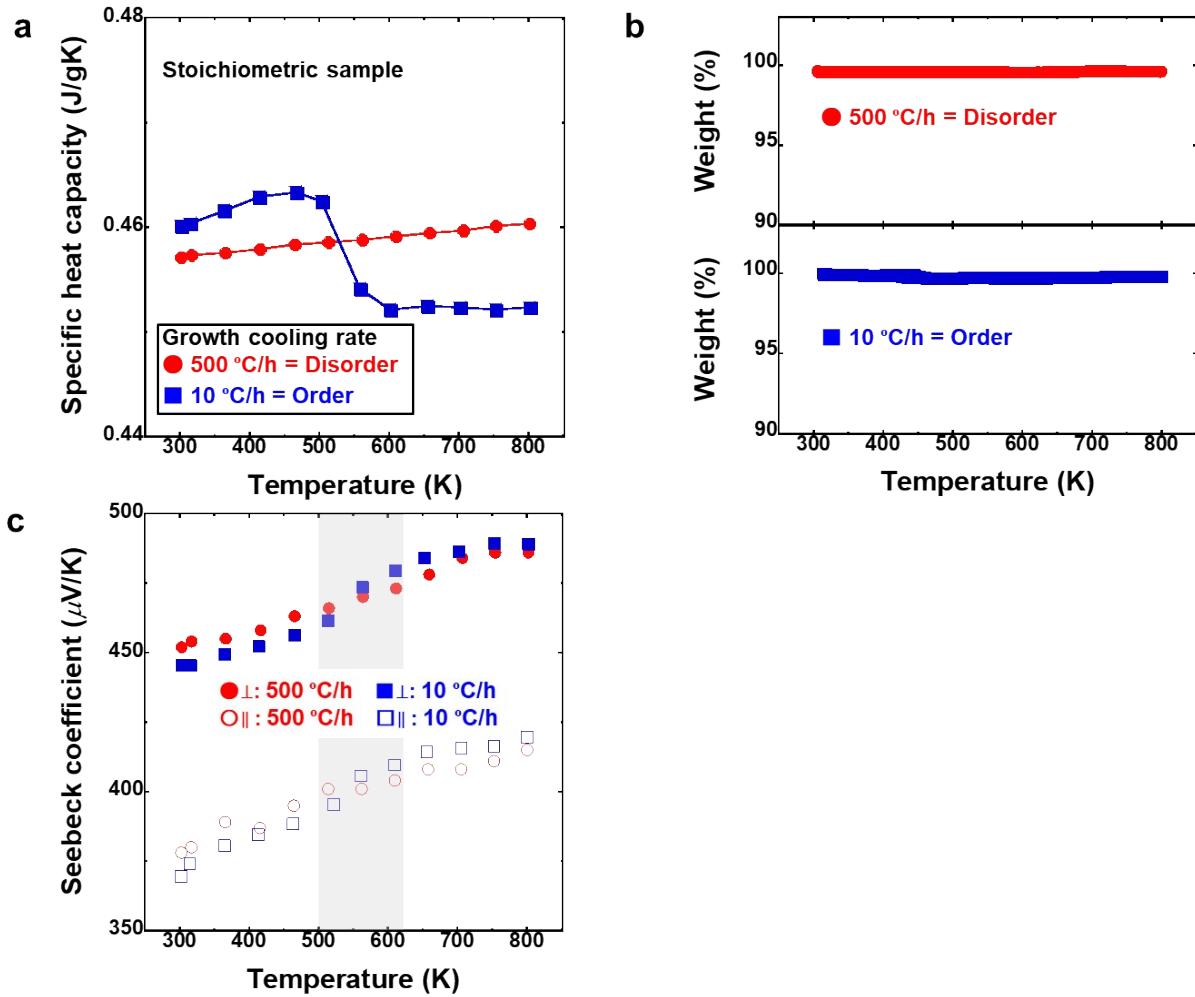
Fig. S4 The observation of ordered-disordered transition in CZTS single crystals. Temperature dependence of (a) specific heat capacity C_p, (b) TGA, (c) Seebeck coefficient S for samples with different cooling rate. The slope for Seebeck coefficient was different between 500 K to 600 K (gray region) near critical transition temperature of 533 K.
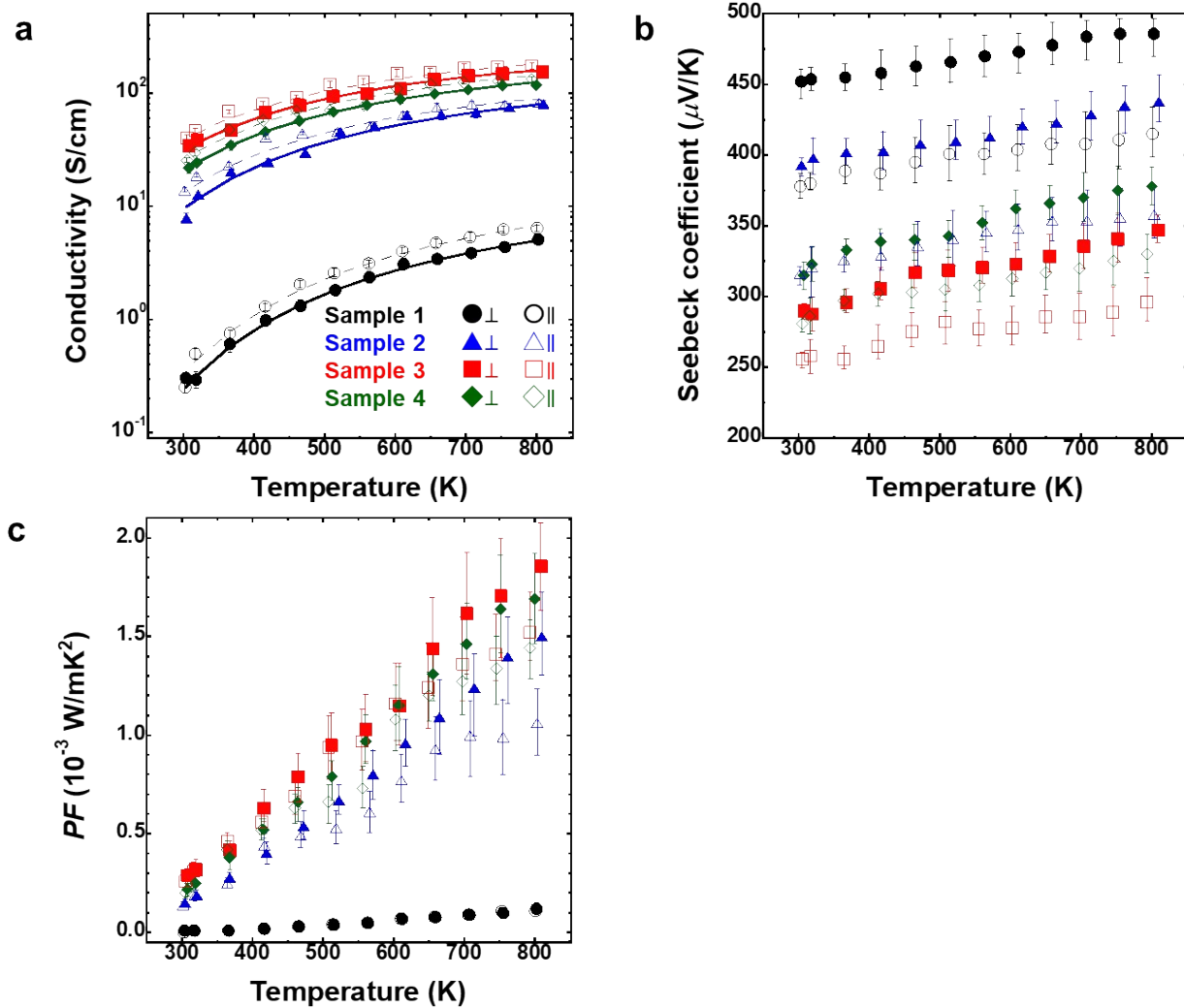
Fig. S5 The reproducibility of TE characterization for CZTS single crystals. Temperature dependence of (a) electrical conductivity σ; (b) Seebeck coefficient S, (c) power factor PF by multiple measurements. The uncertainty of σ is 4-8 % and S is 2-6 %, and the measurement uncertainty of PF is 8-20 %.
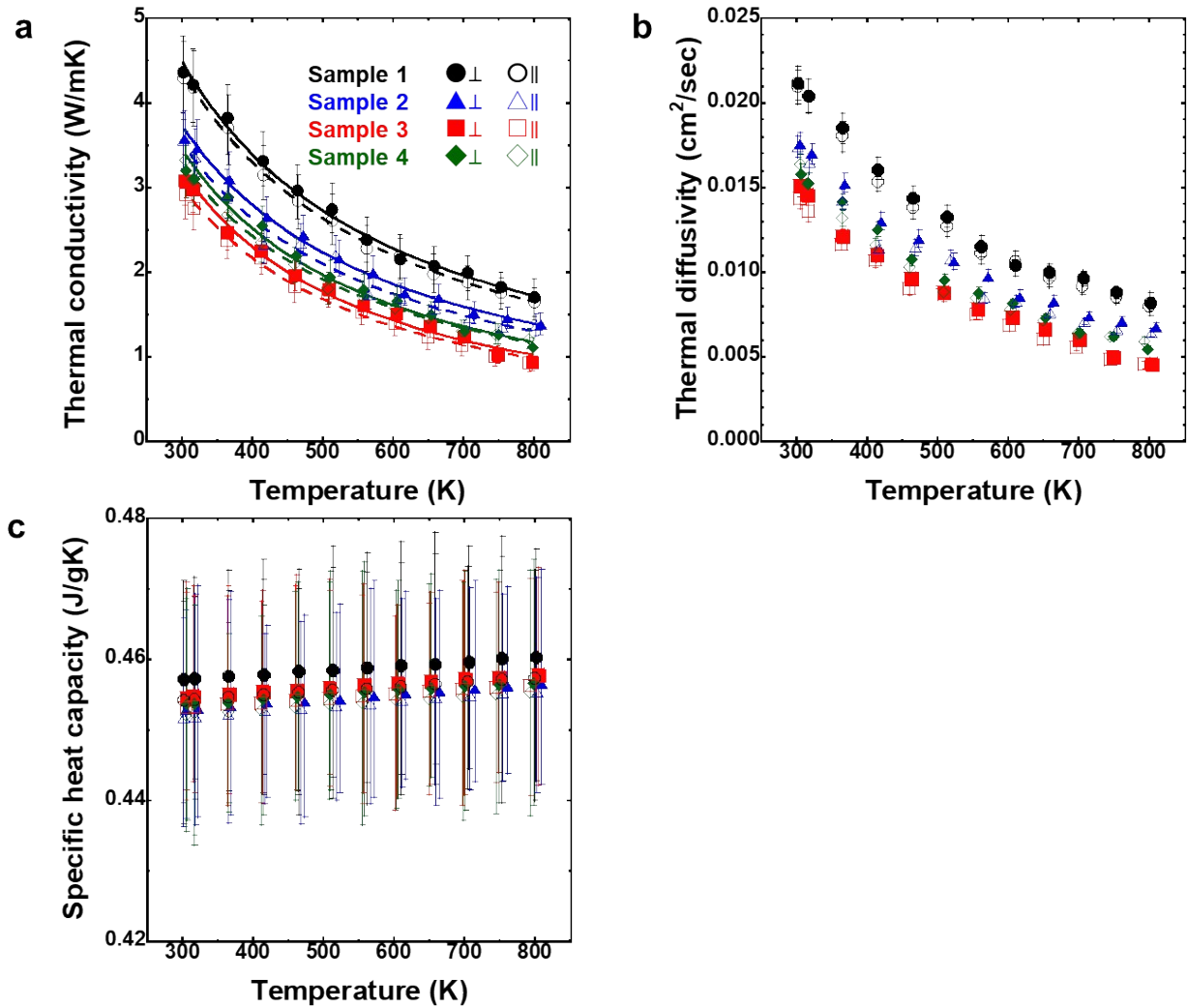
Fig. S6 The reproducibility of thermal transport properties for CZTS single crystals. Temperature dependence of (a) thermal conductivity $\kappa = \lambda C_p D$, (b) thermal diffusivity λ, (c) specific heat capacity C_p by multiple measurements. The density D between 4.4-4.5 g/cm^3 were measured using the Archimedes method at room temperature. The uncertainty of κ is 8-12 % comprising those of 3-5 % for λ, 3-5 % for C_p, and 2 % for D.
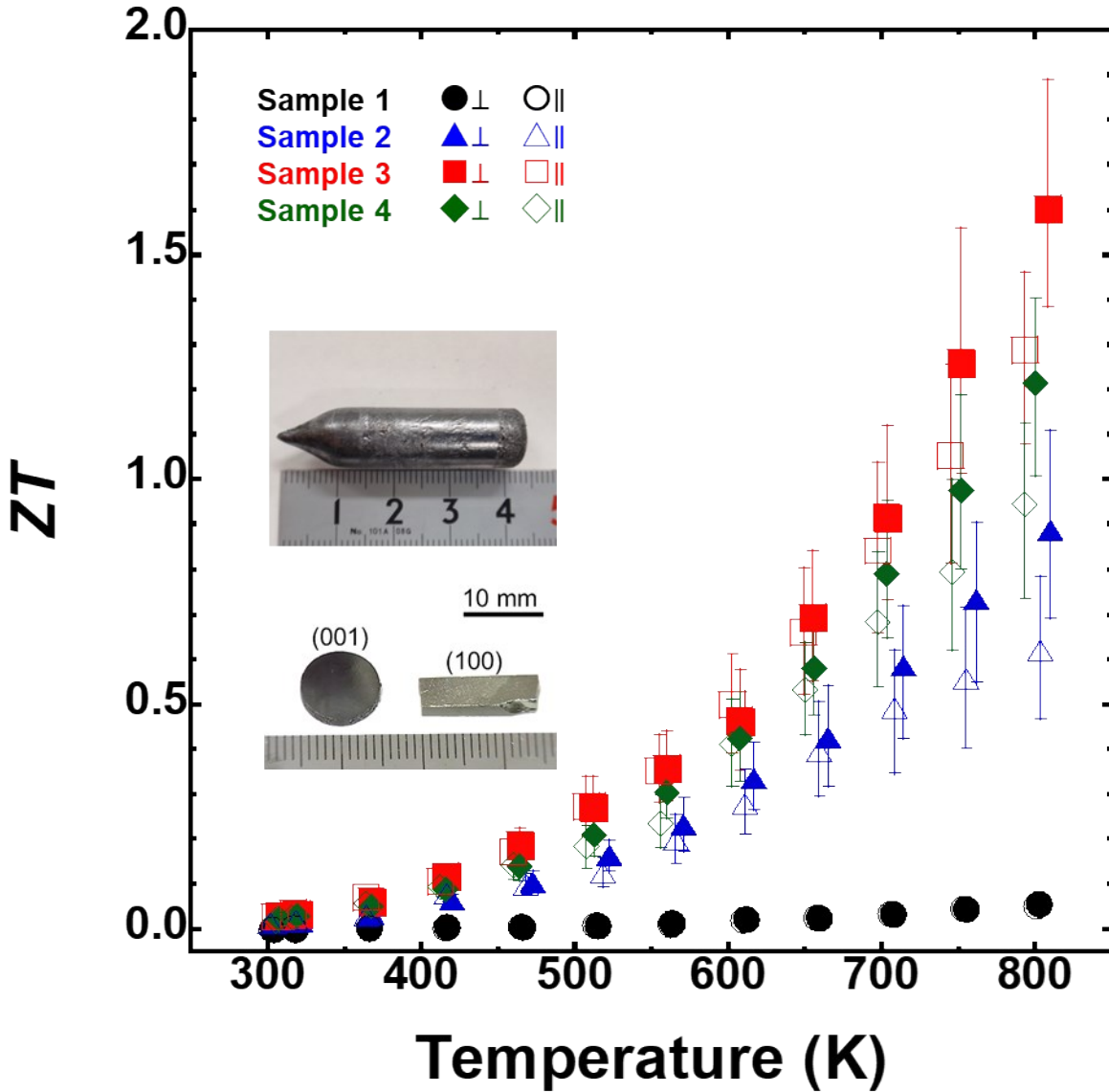
11

Fig. S7 The reproducibility of the dimensionless figure of merit *ZT* for CZTS single crystals. The *ZT* measurement uncertainty is about 30 %.
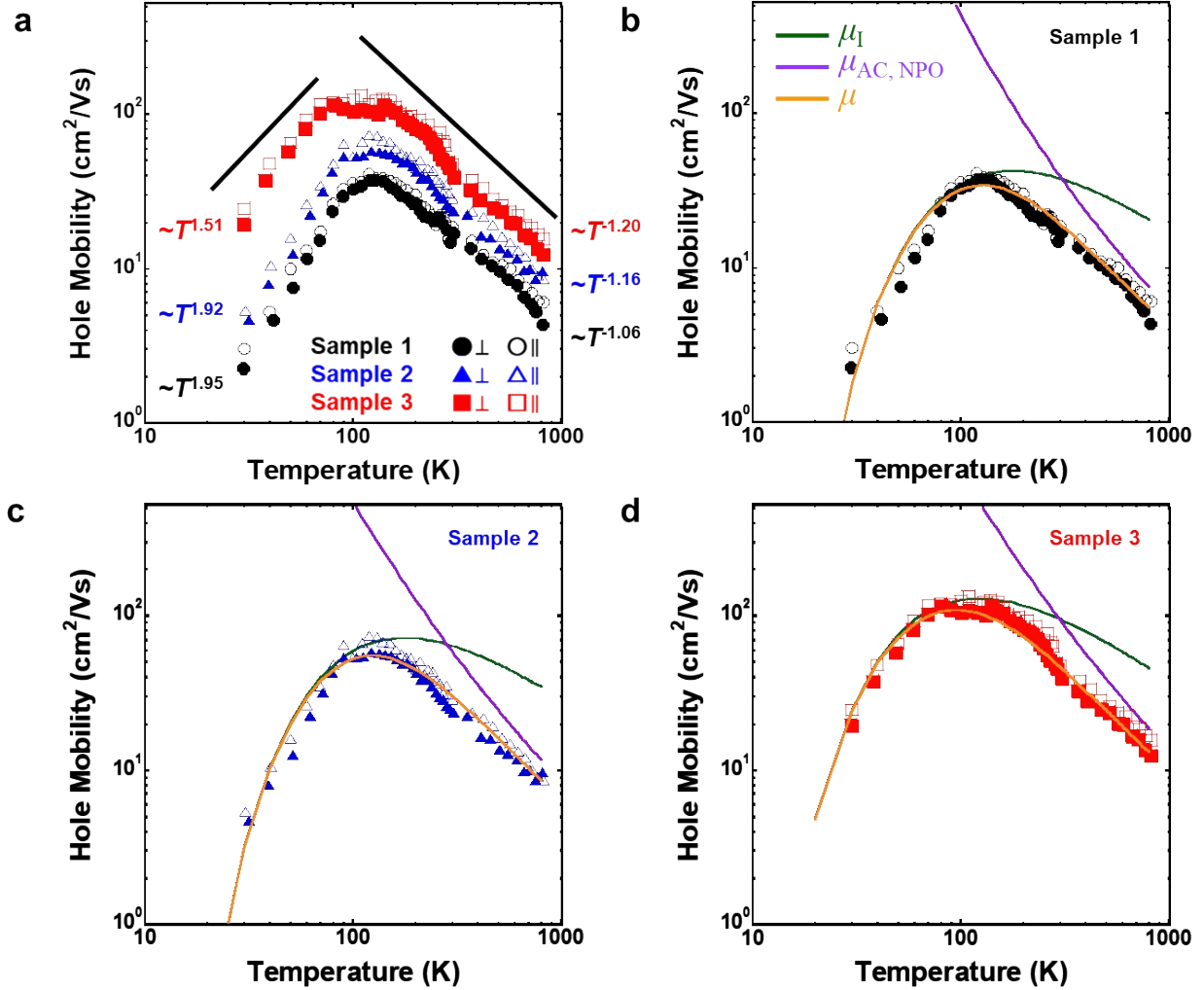
Fig. S8 Temperature dependence of the measured hole mobility in CZTS single crystals. (a) Fitting by T^k relation, (b)-(d) Fitting by the combination of hopping conduction μ_I and acoustic (AC) and non-polar (NPO) phonon scattering $\mu_{AC,NPO}$. The slope parameter k at low temperature $T < 100$ K are higher than 1.5, which indicates hopping conduction in the impurity band. The absolute k values at high temperature $T > 300$ K are less than 1.5 expected for typical lattice scattering. Total hole mobility μ composed of μ_I and $\mu_{AC,NPO}$ is excellent agreement with experimental data.
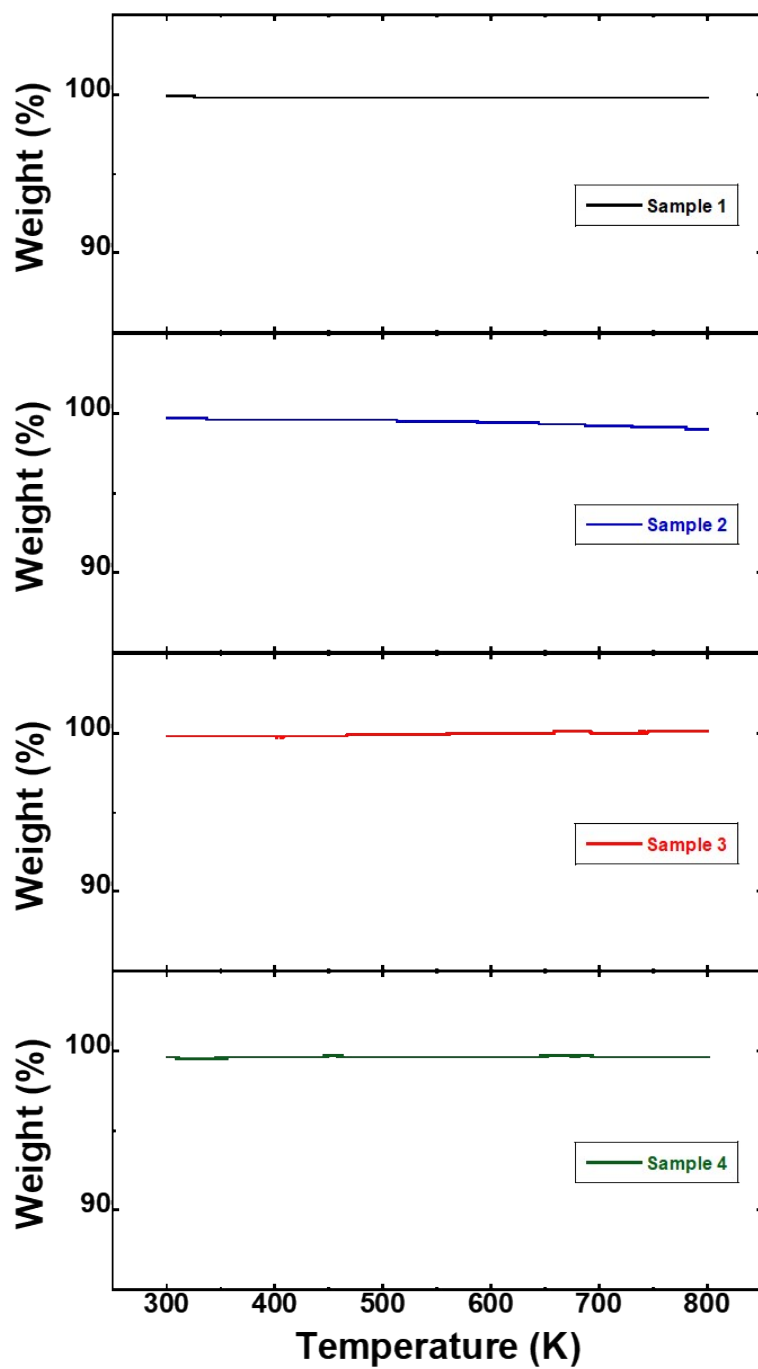
Fig. S9 The TGA measurements of samples 1-4. All samples are stable at the temperature up to 800 K in N_2 atmosphere.
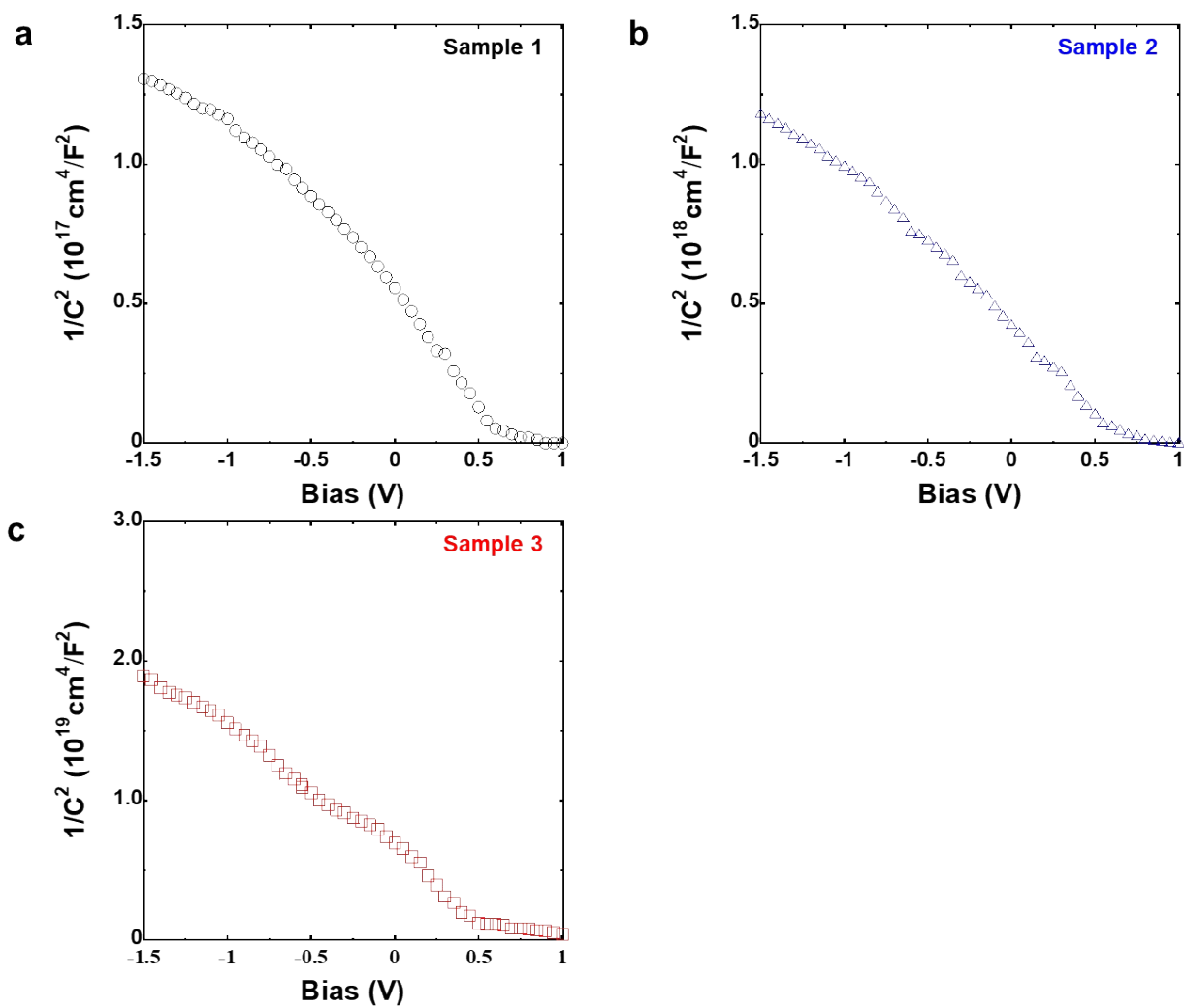
Fig. S10 Mott-Schottky plot for built-in potential estimation at 300 K. (a) sample 1 (stoichiometric), (b) sample 2 (Cu-poor), (c) sample 3 (Na: 0.1 mol%).

a

Cu

S

Zn

Sn

Disordered model

b

Na

Na-doped model
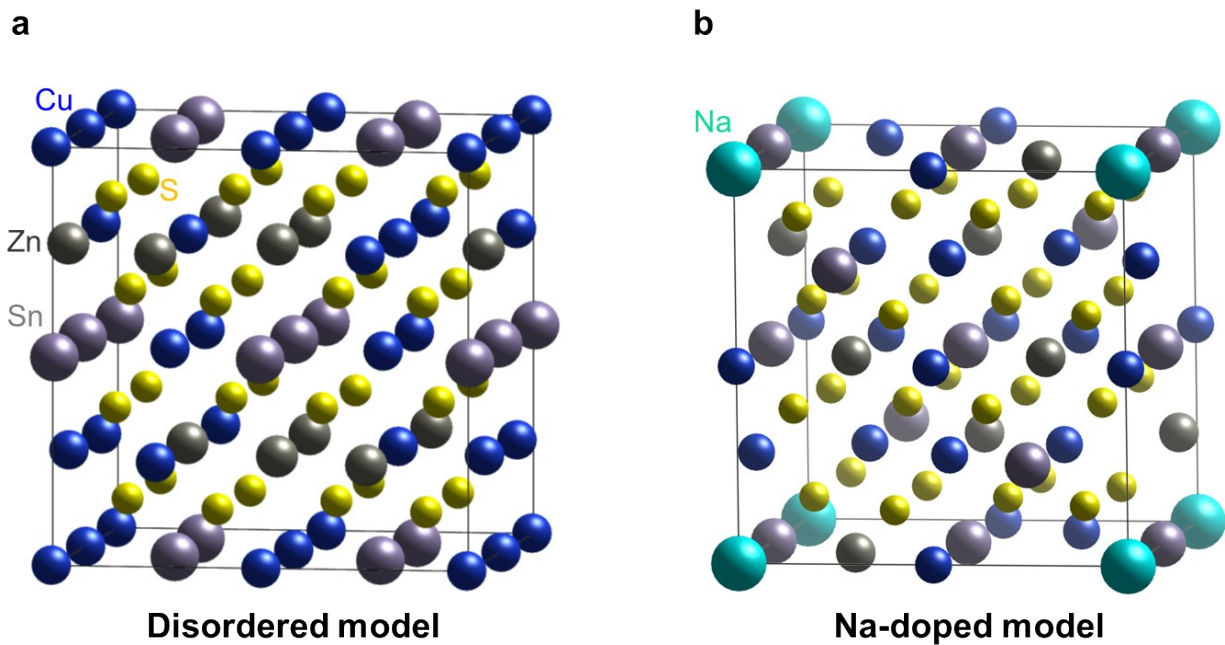
Fig. S11 Supercell crystal structures for DFT calculation. (a) Disordered, (b) 6.25% Na-doped CZTS.
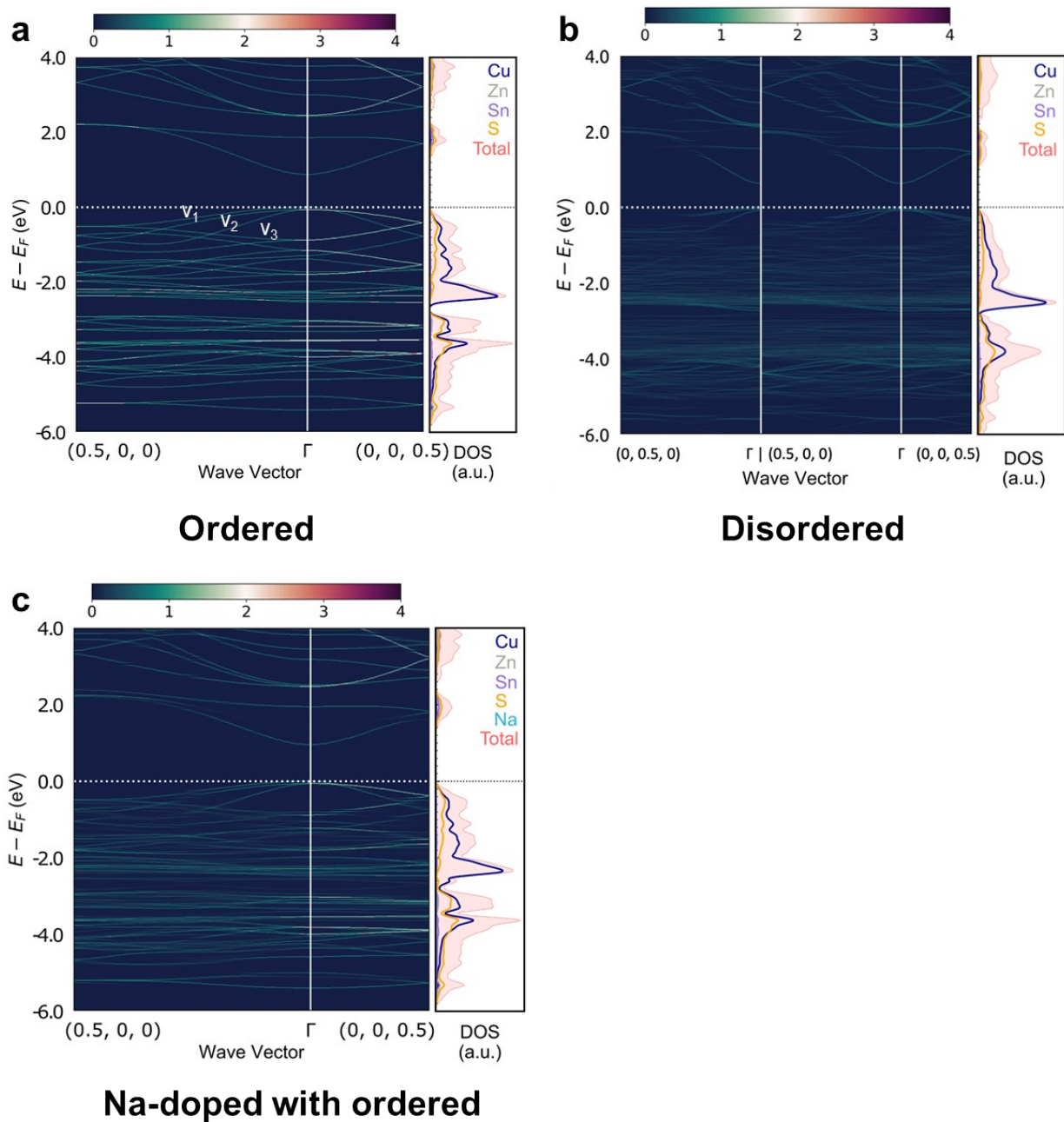
Fig. S12 Electronic band structures of (a) ordered, (b) disordered and (c) Na-doped with ordered CZTS by DFT calculation. The top of the valence band is split into the topmost (v_1) and second (v_2) bands with Γ_{7+8} symmetry and the third band (v_3) with Γ_{5+6} symmetry. Dashed line denotes the Fermi energy E_F. The color scale represents the number of band crossing.

Table S1 The detailed composition of each sample determined by ICP-AES.

	Cu (at.%)	Zn (at.%)	Sn (at.%)	S (at.%)
Sample 1	24.8	12.8	12.3	50.1
Sample 2	23.8	13.3	12.0	50.9
Sample 3	24.2	13.3	12.2	50.3
Sample 4	24.0	13.1	12.3	50.6

Table S2 Unintentional impurity levels detected by ICP-AES in the CZTS single crystals.

Impurity (ppb)	Sample 1	Sample 2	Sample 3	Sample 4
C	430	530	310	320
N	30	25	15	35
O	320	390	270	230
Mg	650	550	450	600
Al	320	180	150	210
Si	230	450	350	320
Ni	60	55	40	50
Fe	45	35	30	20

Table S3 Results and parameters of the CZTS single crystals determined as described in the main text.

	Electrical properties at 300 K			Conduction parameters		AS measurement				
	p (cm^{-3})	σ (S/cm)	μ (cm^2/Vs)	σ_B (S/cm)	E_A (meV)	$E(\omega_0)$ (meV)	Integrated N_t (cm^{-3})	V_bi (V)	2ξ (s^{-1}K^{-2})	W_d (nm)
Sample 1	3.2×10^{16}	0.13	25.1	41	125	100	1.2×10^{16}	0.72	540	252
Sample 2	8.1×10^{17}	6.0	45.4	278	79	80	3.5×10^{17}	0.64	420	220
Sample 3	3.0×10^{18}	42.8	89.3	455	64	65	2.2×10^{18}	0.61	290	198
Sample 4	1.8×10^{18}	26.9	76.9	400	71	73	9.2×10^{17}	0.63	300	205

Table S4 Scattering parameters of the CZTS single crystals determined from temperature dependence of hole mobility.

	H (eVcm^2/Vs)	W (meV)	E_{AC} (eV)	E_{NPO} (eV)	D (g/cm^3)	u (cm/s)	m_{v1}/m_e	θ_D (K)	θ (K)
Sample 1	1.8	15.3	10.0	15.0					
Sample 2	3.0	12.4	10.0	13.0	4.405	2.84×10^5	0.47	302	310
Sample 3	3.7	10.5	8.0	12.0					

Table S5 High temperature TE properties of CZTS single crystal compared to some relating quaternary materials.

Material	σ (S/cm)	S (μV/K)	PF (10^{-3}W/mK^2)	κ (W/mK)	ZT	T_{ZT} (K)	Ref.
Sample 3	165	347	1.86	0.95	1.6	800	This work
$Cu_{2.125}Zn_{0.875}SnS_4$	197	153	0.46	0.31	1.07	723	S10
$Cu_{2.19}Zn_{0.8}Sn_{0.75}S_{3.53}$	13.9	301	0.125	0.645	0.14	700	S11
$Cu_2ZnSn_{0.9}In_{0.1}Se_4$	102	300	0.92	0.82	0.95	850	S12
$Cu_{2.2}Zn_{0.8}SnSe_4$	157	192	0.58	0.54	0.86	800	S13
$Cu_{2.15}Cd_{0.85}SnSe_{3.9}$	67	180	0.22	0.21	0.71	685	S14
$Cu_2CoSnSe_4$	130	230	0.69	0.84	0.7	850	S15
$Cu_{2.15}Zn_{0.85}GeSe_{3.9}$	206	120	0.30	0.4	0.55	723	S16
$Cu_2MnSnSe_4$	52	270	0.37	0.6	0.52	850	S15
$Cu_2Zn_{0.4}Fe_{0.6}SnSe_4$	75	232	0.40	0.7	0.46	800	S17
$Cu_2FeSnSe_4$	64	235	0.35	0.75	0.4	850	S15

Table S6 Anisotropy of the effective hole masses (m_n for n = v_1, v_2, and v_3 in Fig. S11) in ordered, disordered and Na-doped CZTS. m_e is electron mass. The transverse $\perp$ masses are determined from the energy dispersions in (100) direction, and the longitudinal $\parallel$ masses are determined from the dispersions in (001) direction.

	$m_{v1}^{\perp}[m_e]$	$m_{v1}^{\parallel}[m_e]$	$m_{v2}^{\perp}[m_e]$	$m_{v2}^{\parallel}[m_e]$	$m_{v3}^{\perp}[m_e]$	$m_{v3}^{\parallel}[m_e]$
Ordered	0.77	0.17	0.78	0.76	0.16	0.76
Disordered	0.83	0.18	0.54	0.72	0.35	0.73
Na-doped	0.81	0.17	0.84	0.79	0.17	0.79

Supplementary References

S1. I. D. Olekseyuk, I. V. Dudchak, and L. V. Piskach, *J. Alloy. Compd.*, 2004, **368**, 135-143.

S2. A. Nagaoka, K. Yoshino, H. Taniguchi, T. Taniyama and H. Miyake, *J. Crystal Growth*, 2012, **341**, 38-41.

S3. A. Nagaoka, M. A. Scarpulla, and K. Yoshino, *J. Crystal Growth*, 2016, **453**, 119-123.

S4. J. J. S. Scragg, L. Choubrac, A. Lafond, T. Ericson, and C. Platzer-Björkman, *Appl. Phys. Lett.*, 2014, **104**, 041911.

S5. E. Isotta, B. Mukherjee, C. Fanciulli, N. M. Pugno, and P. Scardi, *J. Phys. Chem. C*, 2020, **124**, 7091-7096.

S6. A. Nagaoka, H. Miyake, T. Taniyama, K. Kakimoto, and K. Yoshino, *Appl. Phys. Lett.*, 2013, **103**, 112107.

S7. A. Nagaoka, H. Miyake, T. Taniyama, K. Kakimoto, Y. Nose, M. A. Scarpulla, and K. Yoshino, *Appl. Phys. Lett.*, 2014, **104**, 152101.

S8. M. Cutler, and N. F. Mott, *Phys. Rev.*, 1969, **181**, 1336.

S9. J. D. Wiley, and M. DiDomenico, Jr, *Phys. Rev. B*, 1970, **2**, 427.

S10. Q. Jiang, H. Yan, Y. Lin, Y. Shen, J. Yang, and M. J. Reece, *J. Mater. Chem. A*, 2020, **8**, 10909-10916.

S11. H. Yang, L. A. Jauregui, G. Zhang, Y. P. Chen, and Y. Wu, *Nano Lett.*, 2012, **12**, 540-545.

S12. X. Y. Shi, F. Q. Huang, M. L. Liu, and L. D. Chen, *Appl. Phys. Lett.*, 2009, **94**, 122103.

S13. Y. Dong, H. Wang, and G. S. Nolas, *Phys. Status Solidi RRL*, 2014, **8**, 61-64.

S14. M. Ibáñez, D. Cadavid, R. Zamani, N. G. -Castelló, V. I. -Roca, W. Li, A. Fairbrother, J. D. Prades, A. Shavel, J. Arbiol, A. P. -Rodríguez, J. R. Morante, and A. Cabot, *Chem. Mater.*, 2012, **24**, 562-570.

S15. Q. Song, P. Qiu, F. Hao, K. Zhao, T. Zhang, D. Ren, X. Shi, and L. Chen, *Adv. Electron. Mater.*, 2016, **2**, 1600312.

S16. M. Ibáñez, R. Zamani, A. LaLonde, D. Cadavid, W. Lin, A. Shavel, J. Arbiol, J. R. Morante, S. Gorsse, G. J. Snyder, and A. Cabot, *J. Am. Chem. Soc.*, 2012, **134**, 4060-4063.

S17. Y. Dong, H. Wang, and G. S. Nolas, *Inorg. Chem.*, 2013, **52**, 14364-14367.